Numerical investigations of CO_2 and N_2 miscible flow as the working fluid in enhanced geothermal systems

Jiawei Li [a], Wanju Yuan [b], Yin Zhang [c], Claudia Cherubini [d, **], Alexander Scheuermann [a], Sergio Andres Galindo Torres [e], Ling Li [e, *]

[a] School of Civil Engineering, University of Queensland, Brisbane, 4072, Australia
[b] Faculty of Engineering and Applied Science, University of Regina, Regina, S4S 0A2, Canada
[c] College of Engineering and Mines, University of Alaska Fairbanks, Fairbanks, 755960, United States
[d] Department of Physics and Earth Sciences, University of Ferrara, Via Saragat 1, 44122, Ferrara, Italy
[e] School of Engineering, Westlake University, Hangzhou, 310024, China

ARTICLE INFO

Keywords:
CO_2 and N_2 miscible flow
Fluids properties
Optimized heat extraction efficiency range
Enhanced geothermal systems

ABSTRACT

In this study, the heat extraction from geothermal reservoirs with the application of CO_2 and N_2 miscible flow as the novel working fluids has been investigated based on the discrete fracture network model. The miscible flow with different CO_2 and N_2 proportions and highly pressure and temperature dependent properties have been integrated into reservoir simulations. The heat production processes for CO_2 and N_2 miscible flow have been simulated with two different discrete fracture networks, which also take the thermal-hydraulic-mechanical (THM) coupling mechanisms into consideration. Based on simulation results, it is revealed that the heat extraction efficiencies show an irregular trend with the increasing proportions of N_2 in the mixture. It is found that the miscible flow with two different N_2 proportions (20% and 40%) can be a more efficient working fluid than the one with larger N_2 proportions. Based on simulation results, cumulative heat production curves that represent ten CO_2 and N_2 proportions can be divided into three categories. Evaluations of relevant permeabilities and effective normal stresses at sample points were made, which contributed to the comprehensive analysis of the heat transfer processes. It is also found that there are reasonable ranges for the miscible flow with different CO_2 and N_2 proportions as working fluids that allows higher heat extraction efficiencies, which are validated by a series of comparisons. Thus, in order to define the humps on the heat extraction efficiency curves, a new concept of the optimized heat extraction efficiency range is proposed and validated. It is proved that fluid properties of the miscible flow with different CO_2 and N_2 proportions and the reservoir temperature determine the optimized heat extraction efficiency range directly. This study proposes the miscible flow of CO_2 and N_2 as the working fluid, which provides a new alternative for geothermal energy production.

1. Introduction

Geothermal energy is one of the most potential renewable energy resources (solar, wind, tides etc.) in the world and global geothermal capacity has reached about 18.4 GW in 2018 [1,2]. The geothermal capacity will reach 32 GW if the geothermal power development plans for all countries are performed as expected [3]. In order to enhance the energy extraction efficiency from geothermal reservoirs, the injection of water and CO_2 as working fluids into deep geothermal reservoirs has been proposed and simulated since the end of the 20th century [4–6]. Water has been used as the initial working fluid for the Enhanced Geothermal Systems (EGS) [6–8]. Then, CO_2 as the working fluid during the EGS process has been developed, which takes CO_2 sequestration in deep geothermal reservoirs into consideration [9–11]. In addition to water and CO_2 as working fluids, N_2 has also been proposed [12,13]. In summary, compared with CO_2, N_2 has the following advantages: 1) Lower costs because N_2 can be readily from air; 2) Higher heat extraction efficiency due to its smaller density and viscosity.

In recent years, many investigations have focused on relevant areas of EGS [14–17]. A numerical study of fluid-rock interactions shows that chemically reactive transportations that combines

* Corresponding author.
** Corresponding author.
E-mail addresses: chrcld@unife.it (C. Cherubini), liling@westlake.edu.cn (L. Li).

minerals dissolution and precipitation will affect reservoir porosity and consequently permeability [18]. The effects of salt precipitation during the EGS process have been investigated in a fractured reservoir model, which reflects that geothermal energy production can be inhibited by salt precipitation in fractures [19]. A rough-walled discrete fracture network model that integrates thermal-hydraulic-mechanical coupling mechanisms has been used to analyse heat extraction performance of water and CO_2 as working fluids during the EGS process [20]. A new EGS model that defines several injection and production wells in different reservoir layers has higher heat extraction efficiencies than that of EGS model with two vertical wells [21]. The heat performance of EGS in heterogenous reservoirs has been investigated and a quantified method has been established to predict heat performance [22]. Juliusson et al. [23] have developed an optimization method that is based on maximizing production revenue from fractured geothermal reservoirs.

CO_2 as the working fluid has been utilized to enhance production for different kinds of natural resources (shale gas and oil, conventional gas and oil, gas hydrate, geothermal, etc.) [24–26]. In the area of geothermal energy production, unlike EGS, CO_2 Plume Geothermal (CPG) is also applied for heat extraction from medium and high permeability geothermal reservoirs, which are common in the world and allow an efficient heat exchange between reservoir rocks and working fluids [27–29]. CO_2 has been proposed as the fracturing fluid for shale gas and oil reservoirs and recent studies are mainly relevant to CO_2 flow through single fracture and fracture networks and corresponding processes of fracture propagation [30–33]. There have been several investigations on methane displacement from gas hydrate with the application of CO_2 through experimental and numerical methods [34–36]. Compared with above natural resources, the method of CO_2 flooding to enhance oil recovery in conventional oil reservoirs is the most mature CO_2 utilization in the area of natural resources and has been widely applied in many field projects all over the world in recent decades, which plays an important role in residual oil production [37–40].

In 2015, N_2 as the working fluid for heat extraction from geothermal reservoirs has been simulated and compared with CO_2 [13]. Though there are few studies on the application of N_2 for geothermal energy production, experimental and simulation results of N_2 and CO_2–N_2 mixtures that are used for enhanced oil and gas recovery (EOR) have been presented [41–43]. The solubility and displacement efficiency of N_2 and CO_2 under different contact angles have been investigated through visualization experiments [44]. In a study, N_2 has been added into supercritical CO_2, which contributes to generate the driven foam for enhanced oil recovery [45]. The effects of CO_2–N_2 mixtures on minimum miscibility pressure for targeted oil have been evaluated through detailed comparisons [46]. Seomoon et al. [47] have simulated the injection of CO_2–N_2 mixtures into coal seam for methane production with considering diffusion phenomenon.

A great advantage for CO_2 as the working fluid to be utilized in the area of natural resources production is CO_2 sequestration in the reservoir during the production process, which cannot be ignored and is very important for global environment [48–51]. CO_2 sequestration in geothermal reservoirs has been investigated while geothermal energy is being extracted [52–54]. In this paper, the miscible flow with different CO_2 and N_2 proportions through discrete fracture networks in geothermal reservoirs are simulated.

2. Model descriptions

2.1. Fluids properties

This study mainly focuses on the effects of different CO_2 and N_2 proportions in the miscible flow on heat extraction performance. Ten different proportions of N_2 from 5% to 50% with a constant increasing value of 5% and corresponding proportions of CO_2 in the miscible flow have been used as working fluids for numerical simulations respectively. The properties of the miscible flow have physical continuities though the transformation of the miscible flow states may occur, such as gas to liquid state under reservoir conditions in this study.

Combined with relevant equations and empirical correlations, Peng-Robinson Equation of State is adopted to perform calculations of highly pressure and temperature dependent properties of the miscible flow for different proportions. The properties of the miscible flow (density, viscosity and heat capacity) can be expressed as functions of pressure and temperature that will be applied for further simulations in this study.

2.2. Model assumptions

In this study, a dual porosity reservoir model is established with one injection well locating on the left boundary and one production well locating on the right boundary. A simple schematic is shown in Fig. 1 [55]. A discrete fracture network and rock matrix constitute the target reservoir. Based on the mass and energy balance theories, four basic assumptions are made for the development of the mathematical model:

1) The rock matrix of the reservoir model has isotropic properties. And the permeability of the rock matrix is very small that can be ignored, which means that the rock matrix could be almost impermeable.
2) Darcy Law's is applicable to describe fluid flow in the reservoir.
3) The original fluid in the reservoir is the same as the injected working fluid and no water exists.
4) Under the reservoir conditions (the temperature range 20–150°c, the pressure range 56.35–60.27 MPa), the miscible CO_2 and N_2 flow has two states of matter: gas and liquid. With

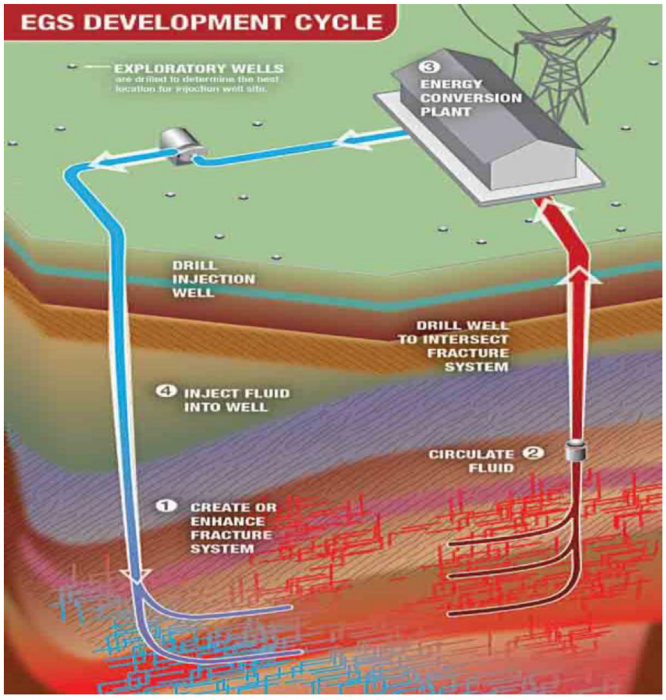

Fig. 1. EGS Schematic with one injection and one production well [55].

considering the continuous properties of changing phases for the miscible flow and large densities (from 600 to 1200 kg/m^3), the miscible flow in the reservoir is simplified as the liquid flow.

5) Only CO_2 and N_2 exist. And the sum of CO_2 and N_2 proportions in the miscible flow equals 100%.

2.3. Governing equations

Based on previous studies, the governing equations in the mathematical model are demonstrated in the following section [56–59]. On the basis of initial assumptions, the permeability of the rock matrix is much lower than that of the fractures, which means that the fluid velocity in the rock matrix is so small as to be negligible. Thus, the temperature of the fluids in rock matrix equals to the one in the reservoir. The mass equations and the Darcy velocity in the rock matrix are expressed in the following forms [56]:

$$S_m\frac{\partial p}{\partial t}+\nabla\cdot u_m=-\frac{\partial e_m}{\partial t}+Q \tag{1}$$

$$u_m=-\frac{k_m}{\eta_i}(\nabla p+\rho_i g\nabla z) \tag{2}$$

The mass equations and the Darcy velocity that is described by Darcy Law in the fracture are written as [56]:

$$d_f S_f\frac{\partial p}{\partial t}+\nabla_\tau\cdot u_f=d_f\frac{\partial e_f}{\partial t}+Q_f \tag{3}$$

$$u_f=-d_f\frac{k_f}{\eta_i}(\nabla_\tau p+\rho_i g\nabla_\tau z) \tag{4}$$

where S represents the storage coefficient, m represents the rock matrix, f represents the fracture, d_f represents the fracture thickness, u represents the flow rate, e represents the volumetric strain, Q_f represents mass transfer between the fracture and rock matrix, k represents the permeability, η represents the fluid dynamic viscosity, g represents the gravity acceleration, p represents the pressure, t represents the time, z represents a unit vector, φ represents the rock matrix porosity.

The energy conservation equation in the rock matrix is shown [57,58]:

$$(\rho C)_{eff}\frac{\partial T_m}{\partial t}=\lambda_{eff}\nabla^2 T_m \tag{5}$$

$$(\rho C)_{eff}=(1-\varphi)\rho_m C_m+\varphi\rho_f C_f \tag{6}$$

$$\lambda_{eff}=(1-\varphi)\lambda_m+\varphi\lambda_f \tag{7}$$

The energy conservation equation in the fracture is shown [59]:

$$d_f\rho_f C_f\frac{\partial T_f}{\partial t}+d_f\rho_f C_f\cdot u_f\nabla_\tau T_f=\nabla_\tau\cdot\left(d_f\lambda_f\nabla_\tau T_f\right)+h\left(T_m-T_f\right) \tag{8}$$

where T represents the temperature, C represents the specific heat conductivity, λ represents the heat conductivity, h represents the convection heat transfer coefficient. And other parameters for equations that are used are the same to the parameters in mass equations.

The equilibrium equation and the deformation equation of the fracture can be written as [60]:

$$\mu u_{i,jj}+(\lambda+\mu)u_{j,ji}-\alpha_B P_{,i}-K^{'}\alpha_T T_{s,i}+F_i=0 \tag{9}$$

$$\lambda=\frac{E\nu}{(1+\nu)(1-2\nu)} \tag{10}$$

$$\mu=\frac{E}{2+\nu} \tag{11}$$

$$u_n=\frac{\sigma_n^{'}}{k_n},\ u_s=\frac{\sigma_s^{'}}{k_s} \tag{12}$$

$$\sigma_n^{'}=\sigma_n-\alpha_B p,\ \sigma_s^{'}=\sigma_s \tag{13}$$

where $u_{i,jj}$ represents the divergence of the transpose of the Cauchy stress tensor, F_i represents the body force per unit volume in the i-coordinate, $-\alpha_B P_{,i}$ denotes the seepage body force resulting from the pore pressure, λ and μ are Lame's constants, E and ν are elastic modulus and Poisson's ratio respectively, $-K^{'}\alpha_T T_{s,i}$ represents the thermal stress term, in which α_T is the coefficient of volumetric expansion corresponding to the bulk medium.

2.4. Model validations

The governing equations of mass and heat transfer processes through rock matrix and fractures are presented in the Section 2.3. The integration of mass and heat transfer processes is realized through the thermal-hydraulic-mechanical coupling processes in the model. The numerical solutions of this mathematical model are calculated by the finite element method (FEM). The accuracy of the mathematical model proposed in this study needs to be verified before further investigations. In order to verify the proposed model, an analytical method is applied here, which will be compared with the finite element method. Because the 2D discrete fracture network model comprises certain amounts of fractures, a 2D single fracture model that is a much simpler case is used to verify the mass and heat transfer through the rock matrix and fractures. The analytical expression of temperature distributions through a single fracture can be written as [61]:

$$\mathrm{T(x,t)=T_{in}erfc}\left(\frac{\varnothing_e\sqrt{\mathrm{D_e}}}{2\mu\mathrm{d_f}\sqrt{\mathrm{t-x/\mu}}}\mathrm{x}\right) \tag{14}$$

where T_{in} is the injection temperature, $\varnothing_e$ is the effective porosity, D_e is the effective diffusion coefficient, μ is the flow velocity, d_f is the fracture aperture, x is distance from the inlet, t is the time. The effective porosity and diffusion coefficient can be calculated by relevant equations [61].

The 2D single fracture model is shown in Fig. 2. As is shown in Fig. 2, the fluid is injected from the position x = 0 and flows through the single fracture that is surrounded by the rock matrix. The fracture length is 100 m and the fracture aperture that is uniform equals 0.005 m. The parameters for the single fracture model are listed in Table 1. The analytical solutions are calculated by Eq. (8) and numerical solutions are calculated by COMSOL Multiphysics, which is a commercial software based on the finite element method. In Fig. 3-a, analytical and numerical solutions at three sample points (x = 10, 20 and 30 m) along the fracture are compared, which presents pretty matching trends. It can be found that the sample point that is closer to the injection side shows a larger temperature drop because the temperature of the injected fluid is much lower than that of the rock matrix. Fig. 3-b shows that the temperature distributions along the fracture for different

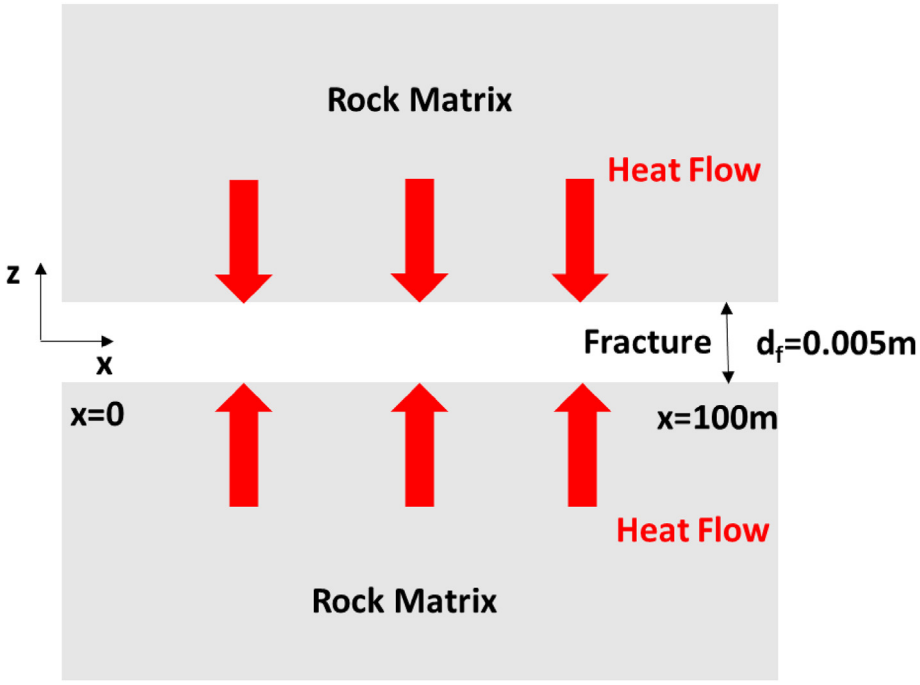

Fig. 2. A simple schematic of heat transfer in a single fracture model.

Table 1
The input parameters for model validations.

Injection velocity μ, m/s	0.01
Injection temperature T_{in}, °c	30
Rock initial temperature T_0, °c	80
Water density ρ_w, kg/m^3	1000
Rock density ρ_r, kg/m^3	2700
Heat conductivity h, W/m^2/K	3000
Fracture aperture d_f, m	0.0005
Water heat capacity C_w, J/kg/K	4200
Rock heat capacity C_r, J/kg/K	1000

injection durations (t = 50, 100 and 150 day) are similar based on analytical and numerical solutions, which reflects that longer injection durations lead to more heat losses. Based on comparisons presented in Fig. 3, the finite element method is verified by the analytical method though very small differences exist. It can be concluded that the finite element method is a reasonable and accurate method to simulate the mathematical model proposed in this paper.

3. Numerical simulation

In this study, a discrete fracture network model made up of parallel plate fractures is used for numerical simulations. As is shown in Fig. 4, two discrete fracture network models are presented, which are marked as Model 1 and 2. The distributions of fracture aperture in Model 1 and 2 is homogenous, having the same value of 5.5×10^{-5} m. And the range of fracture length is between 40 and 60 m. The differences between Model 1 and 2 consists in the fracture densities and inclinations. On the 2D plane, the length of the investigated reservoir is 300 m and the height is 100 m. The depth of the investigated reservoir is assumed to be from 5400 to 5500 m. The main role of Model 2 is to validate simulation results based on Model 1 and provide complementary analysis from the perspective of discrete fracture network constitution.

The initial and boundary conditions of the investigated reservoir are illustrated in the following section. The initial reservoir temperature is set as 150°c. The range of initial reservoir pressure is from 57.82 to 58.8 MPa because gravity is taken into consideration. For example, in Fig. 5, at the top and bottom boundaries 5400 and 5500 m, the corresponding values of initial pressure equal 57.82 and 58.8 MPa separately. With the increasing reservoir depth, the initial reservoir pressure distribution shows a gradual increase due to the effect of gravity. The top and bottom boundaries are assumed to be impermeable and have no heat exchange with other areas. The left and right boundaries represent the injection and production wells. In this study, at the reservoir depth 5400 m, the injecting pressure on the left boundary are set as 56.35, 56.84 and 57.33 MPa and corresponding pressure on the right boundary are 59.29, 58.8 and 58.31 MPa separately. Different reservoir depths result in different pressure values on the left and right boundaries. The injecting temperature for working fluids on the left is set as 20°c. The required reservoir parameters are listed in Table 2.

The main research objective of this study is to investigate the heat extraction performance of the miscible flow of CO_2 and N_2 as working fluids with ten proportions: 1) 95% CO_2 and 5% N_2, 2) 90% CO_2 and 10% N_2, 3) 85% CO_2 and 15% N_2, 4) 80% CO_2 and 20% N_2, 5) 75% CO_2 and 25% N_2, 6) 70% CO_2 and 30% N_2, 7) 65% CO_2 and 35% N_2, 8) 60% CO_2 and 40% N_2, 9) 55% CO_2 and 45% N_2, 10) 50% CO_2 and 50%

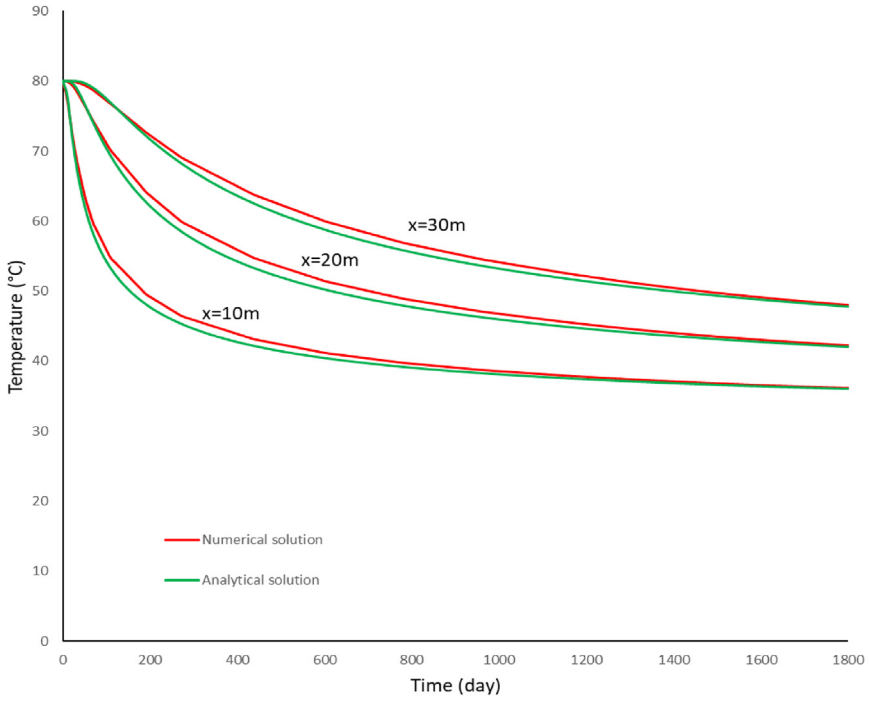

(a) The relationship between temperature and time at three sample points along the fracture

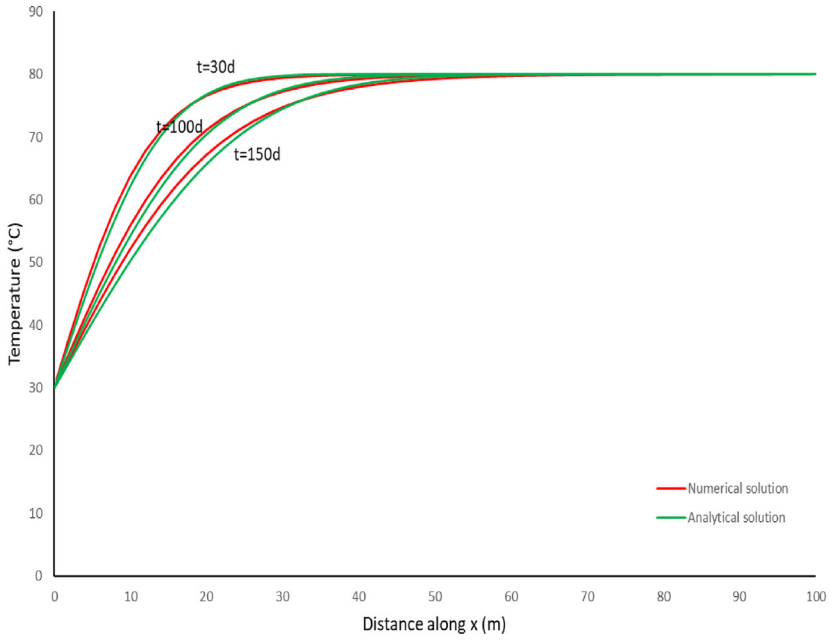

(b) The relationship between temperature and distance along the fracture at three times

Fig. 3. Comparisons between the numerical and analytical solutions in a single fracture model.

N_2. Different proportions of CO_2 and N_2 lead to different fluid properties. In addition, fluid properties are affected by pressure and temperature distributions. In this study, the pressure range is from 56.35 to 60.27 MPa and the temperature range is from 20 to 150°c. In order to reflect the gradual changes of fluid properties, a commercial software CMG WinProp is adopted for relevant calculations based on Peng-Robinson Equation of State. The largest pressure difference for simulating cases in this study is 3.92 MPa, which is about 6.6% change rate. Considering that the temperature range is from 20 to 150°c, the pressure change rate is pretty small compared with the temperature change rate. In addition, fluid properties are very similar at high pressure conditions. Thus, the pressure condition is assumed to be a middle value 58.5 MPa for calculations of fluid properties.

Key fluid properties that contribute to heat extraction performance significantly include density, viscosity and heat capacity.

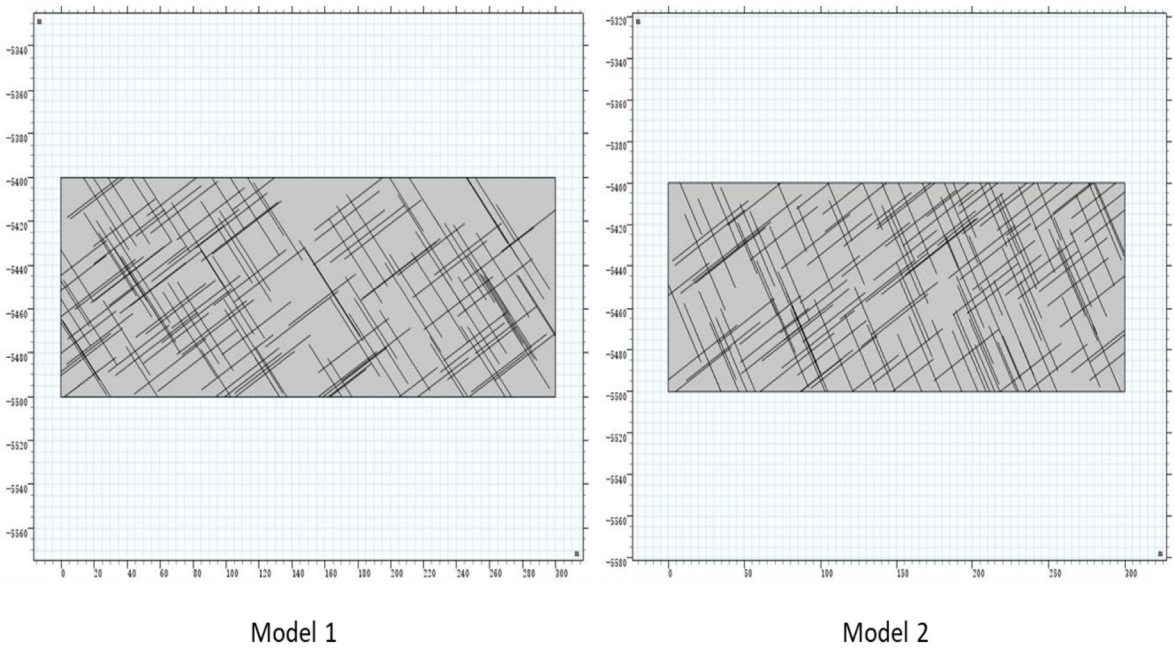

Fig. 4. Schematic of two 2D discrete fracture network models.

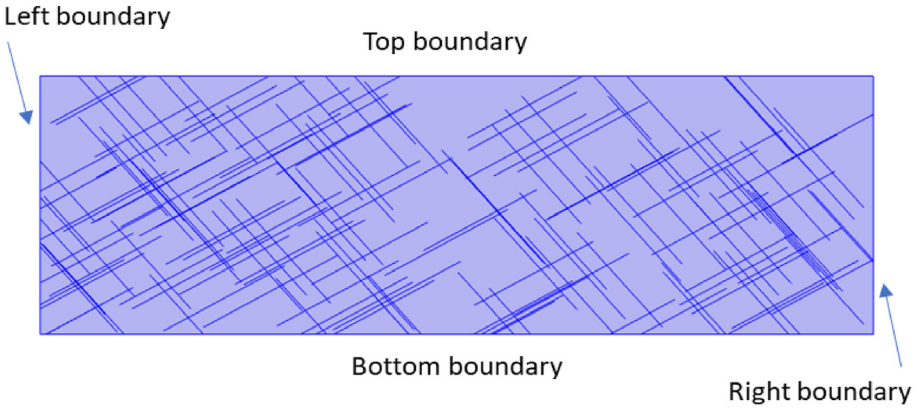

Fig. 5. Reservoir boundaries.

Table 2
Reservoir simulation parameters.

Parameters	Value
Rock density ρ_{rock}, kg/m^3	2800
Rock heat capacity C_S, J/kg/K	1000
Rock thermal conductivity λ_{rock}, W/m/K	3
Rock matrix porosity φ	0.0001
Rock matrix permeability k_m, m^2	1.0×10^{-17}
Convection heat transfer coefficient h, W/m^2/K	2900
Gravity acceleration g, m/s^2	9.8
Elastic modulus E, GPa	30
Poisson ratio η	0.25
Thermal expansion coefficient α_T, K^{-1}	1.0×10^6
Biot's constant α_B	1
Normal stiffness κ_n, GPa/m	1200
Tangential stiffness κ_T, GPa/m	400

Fig. 6 shows densities of different CO_2 and N_2 proportions as a function of temperature (0–150°c) at a constant pressure value 58.5 MPa. For easier expressions in the figure legend, only N_2 proportions are listed because the sum of CO_2 and N_2 proportions in the miscible flow equals 100%. It is observed that the densities of the miscible flow for all investigated proportions have negative relationships with the temperature. With the increase of N_2 proportion in the miscible flow, the density of the miscible flow decreases due to the fact that the mass of N_2 is smaller than that of CO_2. In addition, densities for adjacent N_2 proportions present equal differences, which match the constant increase of N_2 proportions in the miscible flow. In Fig. 7, viscosities for different N_2 proportions show decreasing trends with the increase of temperature. And a larger N_2 proportion lead to a smaller viscosity of the miscible flow. The differences among adjacent N_2 proportions will become smaller while the temperature increases gradually. In Fig. 8, there are humps on relationship curves between heat capacity and temperature that become smaller with the increase of N_2 proportion (0–40%) and finally disappear when the N_2 proportion reaches 45%. When the N_2 proportion equal 45 and 50%, the heat capacity has a linearly decreasing trend with the temperature. Phase transitions occur with the increase of the temperature. For example, the miscible flow of 95% CO_2 and 5% N_2 is still a liquid

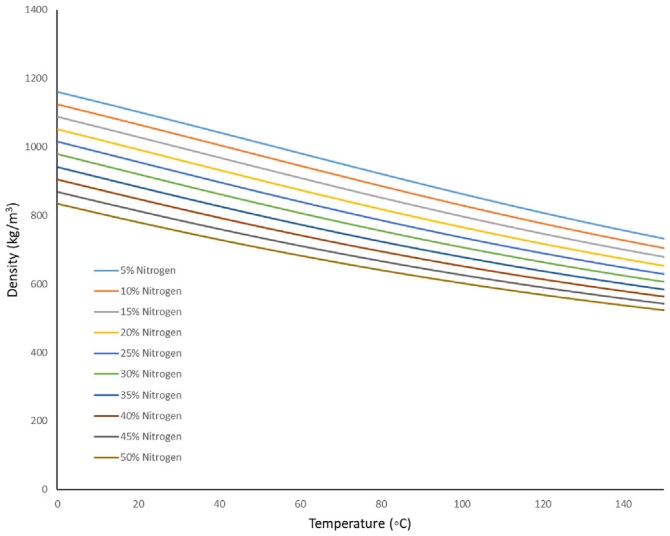

Fig. 6. The relationship between density and temperature for different N_2 proportions at the pressure 58.5 MPa.

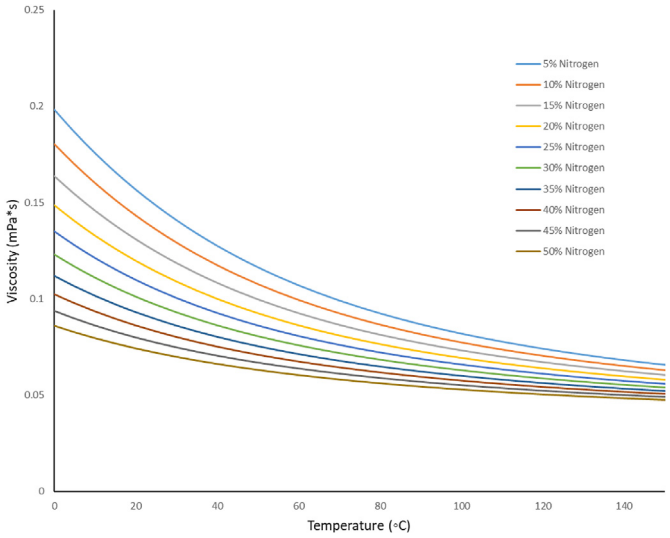

Fig. 7. The relationship between viscosity and temperature for different N_2 proportions at the pressure 58.5 MPa.

phase when the temperature is 20°c. The miscible flow of other proportions in this study remains gas phases when the temperature is above 20°c. It should be noticed that the temperature range for numerical simulations in this study is from 20 to 150°c. In addition, the properties of the miscible flow are continuous though the miscible flow of 95% CO_2 and 5% N_2 is a liquid phase at the temperature 20–25°c. The properties of the miscible flow for different CO_2 and N_2 proportions are used to simulate heat extraction performance from geothermal reservoirs and evaluate the effects of impacting factors.

4. Results analysis

In Figs. 9 and 10, the pressure and temperature distributions of the investigated reservoir with the injection of the 95% CO_2 and 5% N_2 miscible flow at different times are presented. Four different times (3, 10, 15 and 20 year) are adopted in this study. In Fig. 9, it is showed that the pressure distributions for different times are

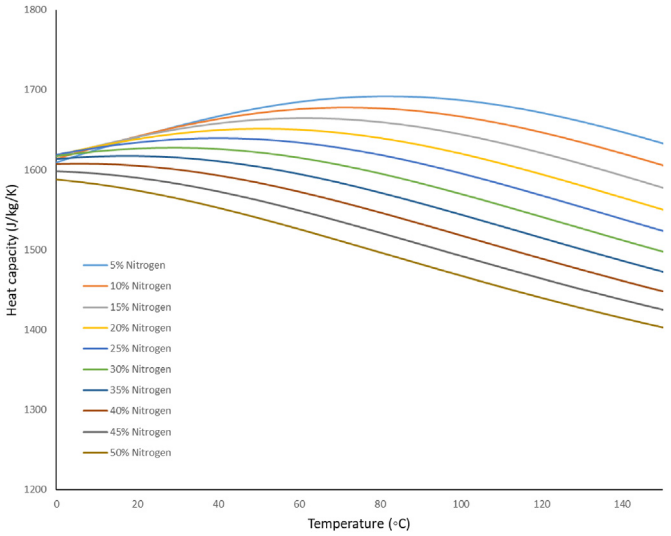

Fig. 8. The relationship between heat capacity and temperature for different N_2 proportions at the pressure 58.5 MPa.

constant, which reflects that the steady state has been reached since the time t = 3 year. It is obvious that the values of pressure decrease from the left side to the right side based on the colour legend. This is because the left and right sides represent the injection and production wells separately. In addition, deeper locations have higher pressure values due the integration of gravity into reservoir simulations. It can be also found that the pressure distributions changes more sharply along fractures because the discrete fracture network is the dominating flow path in the reservoir.

Fig. 10 gives an illustration that the temperature distributions corresponds to pressure distributions in Fig. 9 in the reservoir. From Fig. 10-a to d, it can be observed that blue areas that represent low temperature keep expanding and red areas that represent high temperatures become smaller with time going by. As is shown in Fig. 10-d, red areas eventually disappear and there are only yellow areas instead. The injection of 20°c working fluids on the left side and the production of reservoir fluids on the left side lead to the temperature evolutions in the reservoir. The effects of the discrete fracture network on temperature distributions is more obvious than pressure distributions. In Fig. 10, it can be seen that lower temperature areas are surrounded by higher temperature areas on the interface of different temperature areas, which can be considered as fingering penetrations of lower temperatures.

In Fig. 11, the temperature distributions for different CO_2 and N_2 proportions in the miscible flow at the same time t = 3 year are compared. The temperature distributions in Fig. 11-a is different from those in Fig. 10-b, c and d clearly. In Fig. 11-a, the blue area occupies a small proportion of the total area on the left, which is about between one sixth and one fifth. Though the temperature distributions are pretty similar in Fig. 11-b, c and d, small differences can be observed. By means of comparison among areas surrounded by the red border, it can be found that the 80% CO_2 and 20% N_2 miscible flow lead to faster heat transfer in the reservoir compared with the other three CO_2 and N_2 proportions. The heat transfer of the 50% CO_2 and 50% N_2 miscible flow is a little faster than that of the 65% CO_2 and 35% N_2 miscible flow. The differences in the temperature distributions in Fig. 10 is caused by densities, viscosities and heat capacities of the miscible flow with different CO_2 and N_2 proportions, which have direct effects on heat transfer in the reservoir.

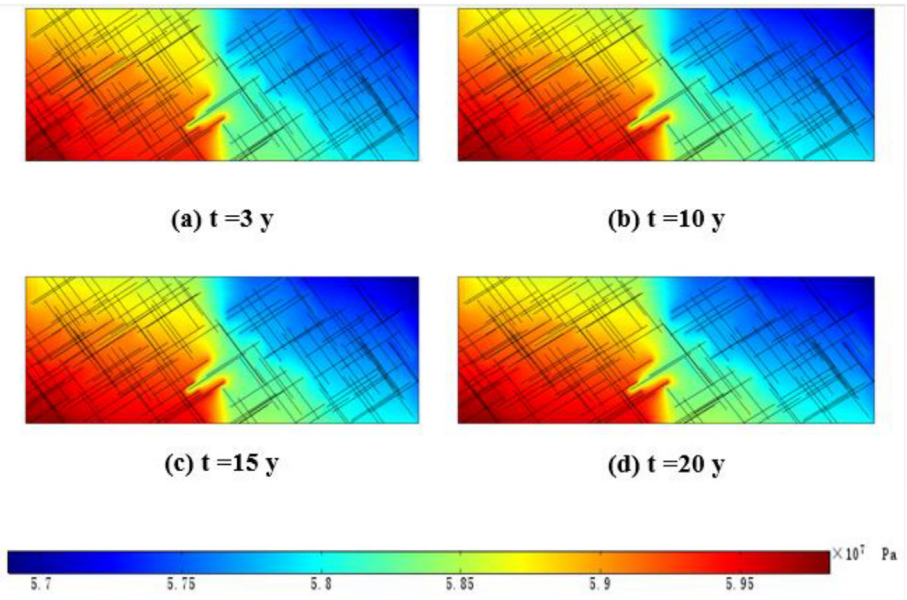

Fig. 9. Pressure distributions with the 95% CO_2 and 5% N_2 miscible flow injection for different times in Model 1.

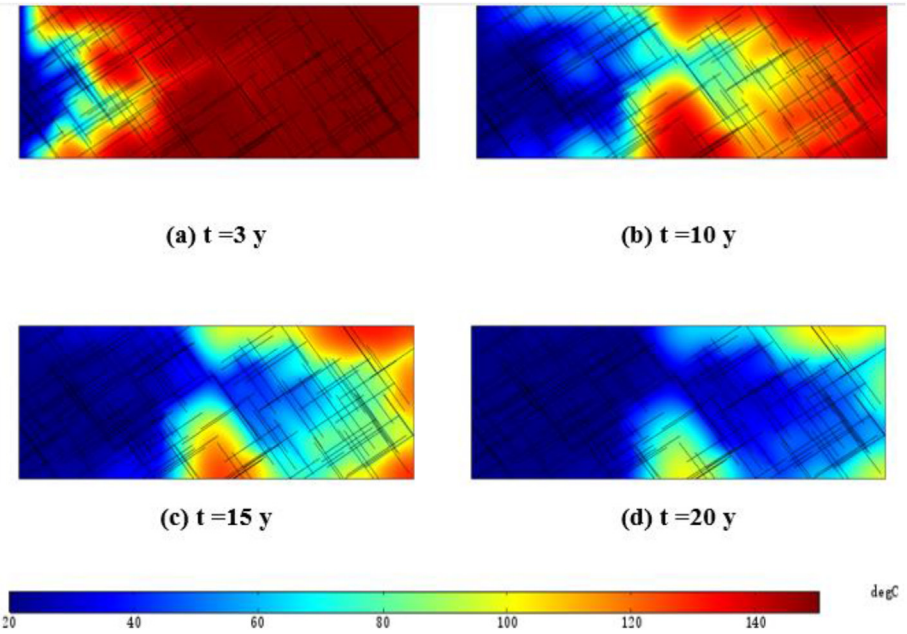

Fig. 10. Temperature distributions with the 95% CO_2 and 5% N_2 miscible flow injection for different times in Model 1.

Fig. 12 is a schematic of three sample points in Model 1 and 2, which is used for the following analysis. Three sample points locate at equally spaced positions (80, 160 and 240 m). Fig. 13 shows the permeability and effective normal stress curves for three sample points with the injection of the 80% CO_2 and 20% N_2 miscible flow in Model 1. The fracture at Point 1 has a larger permeability than those of Point 2 and 3. Point 2 and 3 have closer permeability and effective normal stress curves. With time going by, the permeability curves for Point 1, 2 and 3 keep increasing. The effective normal stress curves strictly correspond to the permeability curves. Fig. 14 presents the permeability and effective normal stress curves for the miscible flow with different CO_2 and N_2 proportions at Point 2. Similarly, the effective normal stress curves match the trends of the permeability curves. It can be found that the miscible flow with 60% CO_2 and 40% N_2 has the largest permeability among ten proportions. The 85% CO_2 and 15% N_2 miscible flow has the smallest permeability. In addition, the permeability and effective normal stress curves can be divided into three parts. The miscible flow with N_2 proportions that are from 5% to 15% have smaller values that locates on the bottom part of Fig. 14 and the miscible flow with 25%, 30% and 35% N_2 proportions has corresponding curves in the middle part. The miscible flow with other four N_2 proportions has larger values of permeability and effective normal stress, which locate above the last-mentioned curves.

In Fig. 15, the permeability and effective normal stress curves for three sample points with the injection of the 80% CO_2 and 20% N_2

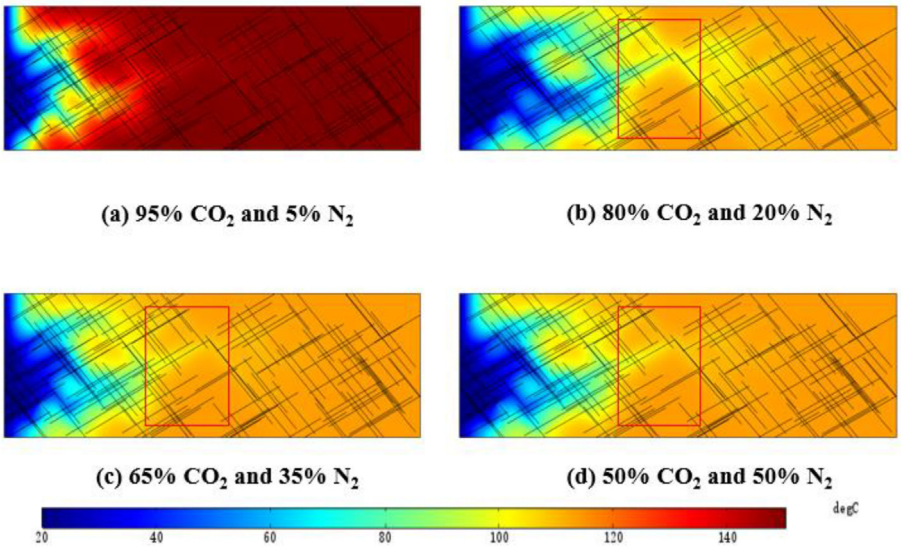

Fig. 11. Temperature distributions for different CO_2 and N_2 proportions in Model 1 when t = 3 year.

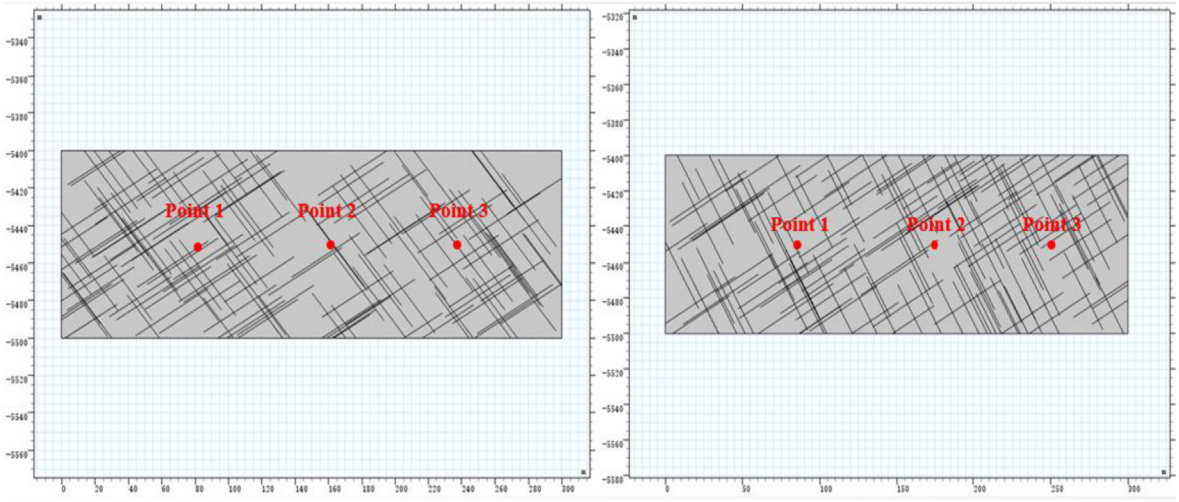

Fig. 12. Three sample points at same locations in Model 1 and 2.

miscible flow in Model 2 are presented. It is shown that Point 1 also has a larger permeability curve than those of Point 2 and 3. However, the permeability and effective normal stress curves of Point 1 and 2 are closer. This is because Model 1 and 2 are different discrete fracture network models. In Fig. 16, the permeability of the 60% CO_2 and 40% N_2 miscible flow are larger than others. The permeability and effective normal stress curves are also divided into three parts based on different N_2 proportions: top (20%, 40%–50%), middle (25%–35%), low (5%–15%), which is coherent with Model 1 in Fig. 14. But the middle part is closer to the top part compared with Model 1 results.

In Figs. 17 and 18, the cumulative heat production for the miscible flow with different CO_2 and N_2 proportions based on Model 1 and 2 are shown. The cumulative heat production curves that represent the miscible flow with different CO_2 and N_2 proportions based on Model 1 and 2 have similar sequences. In Fig. 17, the 60% CO_2 and 40% N_2 miscible flow has the highest cumulative heat production for 20 years. In Fig. 18, the 60% CO_2 and 40% N_2 miscible flow has the highest cumulative heat production for 10 years and then is exceeded by the miscible flow with other proportions. The sequences of cumulative heat production curves in Figs. 17 and 18 strictly follow the permeability and effective normal stress curves in Figs. 14 and 16. As a result, the three parts proposed for Figs. 14 and 16 can be applied to the cumulative heat production curves in Figs. 17 and 18. In addition, the effects of fluids properties are also observed. It is obvious that the spatial differences between the middle and bottom part become smaller in Figs. 17 and 18 compared with the spatial differences in Figs. 14 and 16. This is because the fluid properties (density, viscosity and heat capacity) change with temperature, which are shown in Figs. 6–8. What's more, the sequences of cumulative heat production curves in Figs. 17 and 18 are the same as the permeability curves in Figs. 14 and 16, which reflects that fracture permeability is the most important factor on heat production when the reservoir boundary condition is set as a constant pressure difference in this study. Through comparisons of the same miscible flow, the cumulative heat productions based on Model 2 are higher than those based on the Model 1, which reflects that the total conductivity of Model 2 is

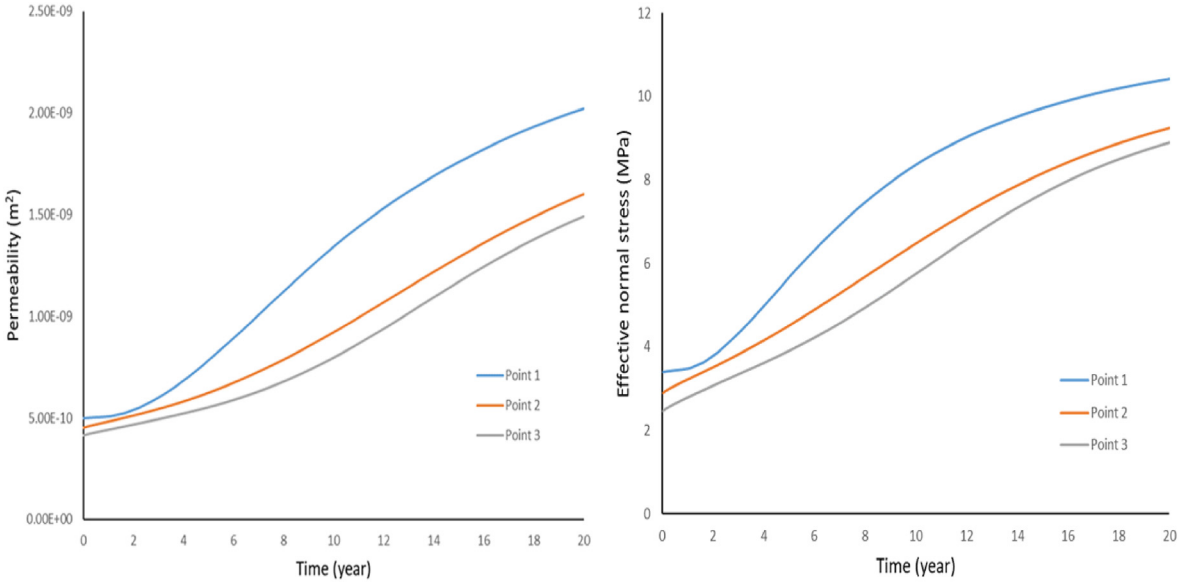

Fig. 13. Permeability and effective normal stress at three sample points in Model 1 with the pressure boundary condition $\Delta p = 1.96$ MPa.

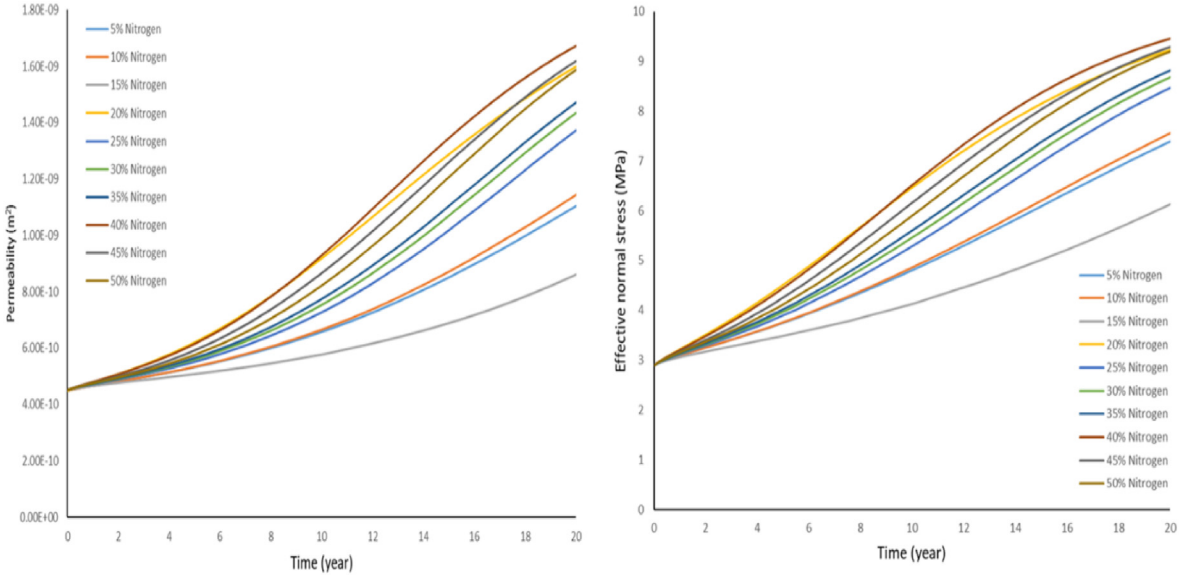

Fig. 14. Permeability and effective normal stress for different CO_2 and N_2 proportions at Point 2 in Model 1 with the pressure boundary condition $\Delta p = 1.96$ MPa.

higher than that of Model 1.

Figs. 19 and 20 display the heat extraction efficiency curves for the miscible flow with different CO_2 and N_2 proportions based on Model 1 and 2 separately. The heat extraction efficiencies based on Model 1 and 2 all have sharp drops at the beginning of production. Sharp drops on the heat extraction efficiency curves are due to the depletion of initial elastic energy in the geothermal reservoir and the pressure supply from the left side that has not reached the right side. Initial conditions of high pressure and temperature result in the existence of initial elastic energy (the hydraulic-thermal-mechanical coupling process has been integrated into the reservoir model in this study).

The appearance of humps on the heat extraction efficiency curves are observed in Figs. 19 and 20. The humps represent ranges of higher heat extraction efficiencies compared with other heat extraction efficiencies during the period of 20 years. The humps on the heat extraction curves can be considered as the optimized heat extraction range. The effects of different CO_2 and N_2 proportions on the appearance of humps are analysed. The top, middle and bottom parts mentioned in the analysis of cumulative heat production contribute to identify appearances of humps on the heat extraction curves. Corresponding to the cumulative heat production, a larger cumulative heat production leads to earlier appearance of humps on the heat extraction curves. For example, the humps of the miscible flow with N_2 proportions (5%—15%) are not clear in Fig. 19 but they can be identified easily in Fig. 20. This is because Model 2 has a higher conductivity than Model 1. When enough heat is produced from the reservoir and the reservoir temperature decreases to a critical value, the humps will appear.

It is also shown that there are small fluctuations on the heat extraction efficiency curves in both Figs. 19 and 20. This is because ongoing heat extraction processes affect temperature distributions

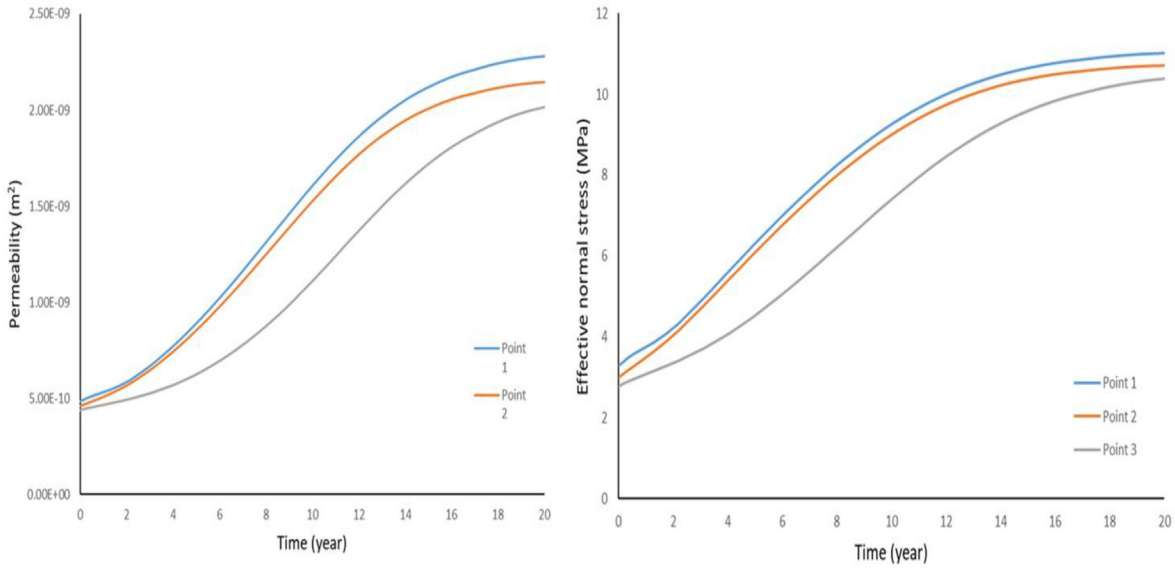

Fig. 15. Permeability and effective normal stress at three sample points in Model 2 with the pressure boundary condition $\Delta p = 1.96$ MPa.

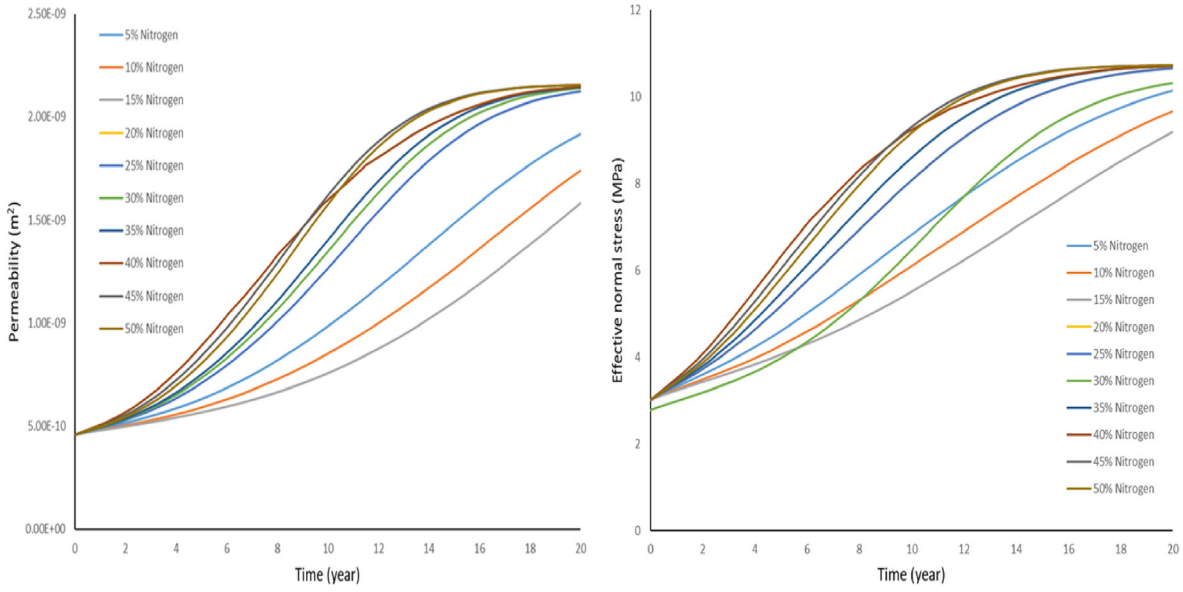

Fig. 16. Permeability and effective normal stress for different CO_2 and N_2 proportions at Point 2 in Model 2 with the pressure boundary condition $\Delta p = 1.96$ MPa.

in the reservoir and densities, viscosities and heat capacities of the miscible flow with different CO_2 and N_2 keep changing with temperature. Though small fluctuations exist, the trends of the heat extraction efficiency curves are not affected.

Figs. 21 and 22 show the cumulative heat production curves generated on Model 1 under the pressure boundary condition $\Delta p = 0.98$ and 2.94 MPa separately, which are compared with the results in Fig. 17. It is observed that the cumulative heat curves in

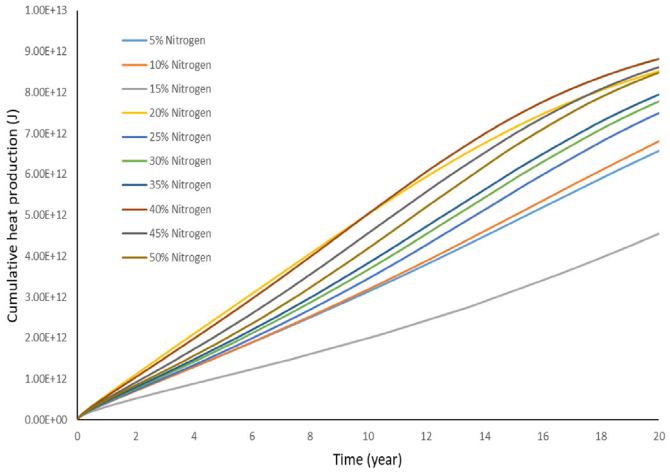

Fig. 17. Cumulative heat production for different CO_2 and N_2 proportions based on Model 1 with the pressure boundary condition $\Delta p = 1.96$ MPa.

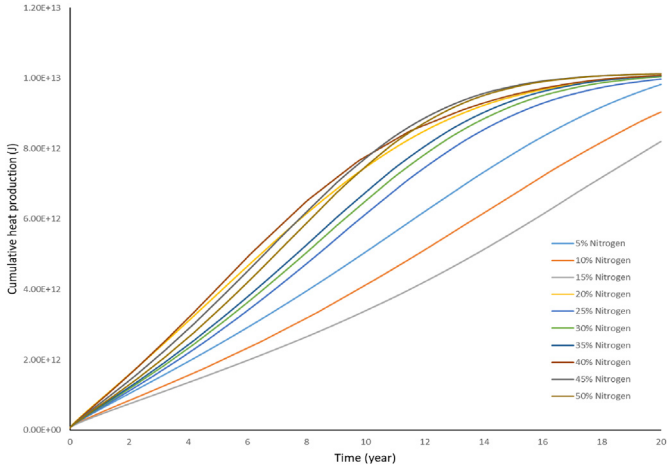

Fig. 18. Cumulative heat production for different CO_2 and N_2 proportions based on Model 2 with the pressure boundary condition $\Delta p = 1.96$ MPa.

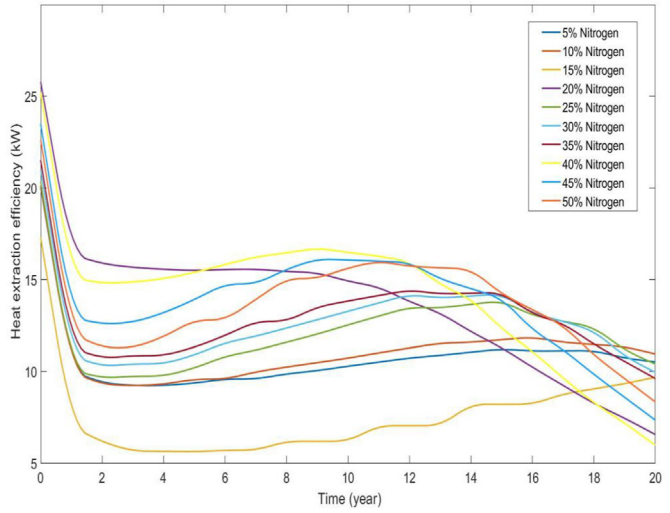

Fig. 19. Heat extraction efficiency curves for different CO_2 and N_2 proportions based on Model 1 with the pressure boundary condition $\Delta p = 1.96$ MPa.

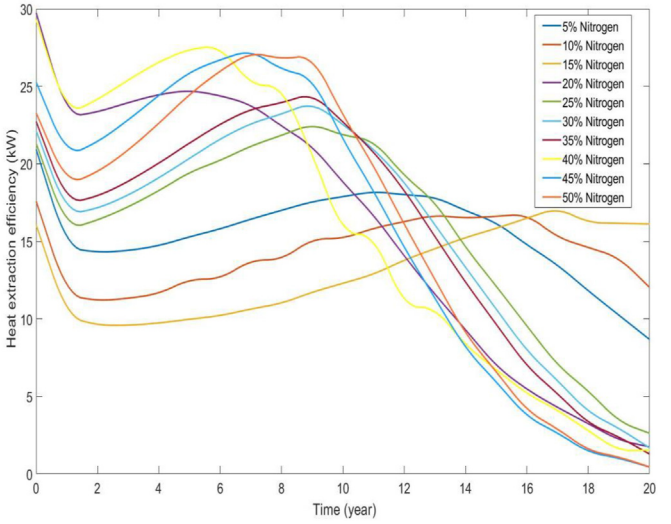

Fig. 20. Heat extraction efficiency curves for different CO_2 and N_2 proportions based on Model 2 with the pressure boundary condition $\Delta p = 1.96$ MPa.

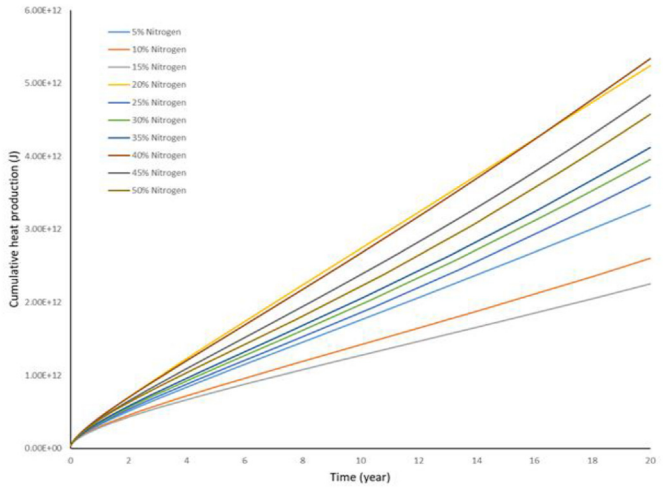

Fig. 21. Cumulative heat production for different CO_2 and N_2 proportions based on Model 1 with the pressure boundary condition $\Delta p = 0.98$ MPa.

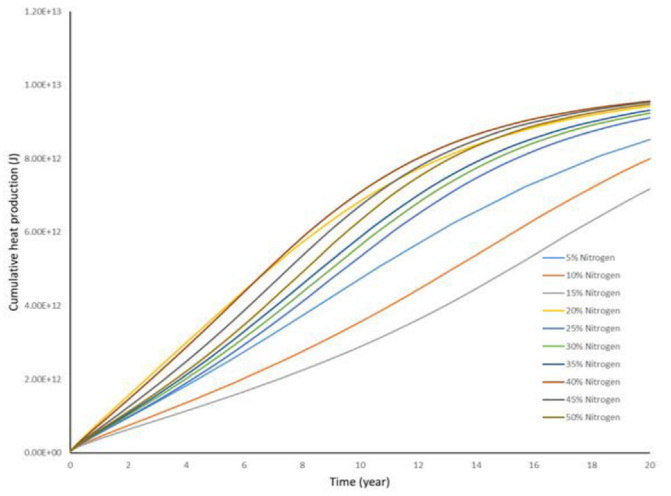

Fig. 22. Cumulative heat production for different CO_2 and N_2 proportions based on Model 1 with the pressure boundary condition $\Delta p = 2.94$ MPa.

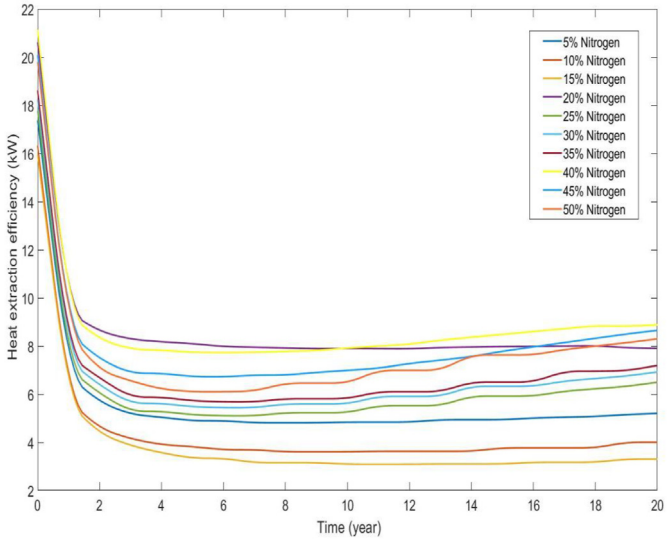

Fig. 23. Heat extraction efficiency curves for different CO_2 and N_2 proportions based on Model 1 with the pressure boundary condition $\Delta p = 0.98$ MPa.

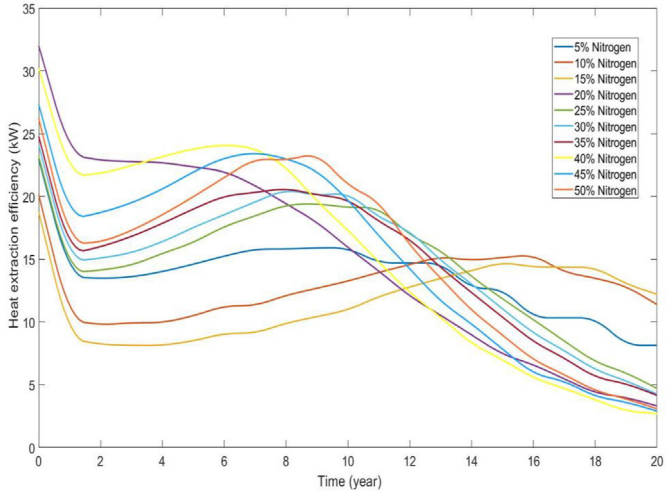

Fig. 24. Heat extraction efficiency curves for different CO_2 and N_2 proportions based on Model 1 with the pressure boundary condition $\Delta p = 2.94$ MPa.

Figs. 21 and 22 have same sequences as the cumulative heat production curves in Fig. 17 for different CO_2 and N_2 proportions. In Fig. 21, the cumulative heat production has a linear relationship with time. In Fig. 22, it is found that cumulative heat production curves for several CO_2 and N_2 proportions have reached very gentle slopes, which means that there is not much geothermal energy left in the reservoir and heat extraction efficiencies are pretty low. Compared with the cumulative heat production curves in Figs. 21 and 22, it can be found that the cumulative heat production curves in Fig. 17 are transitions between corresponding curves in Figs. 21 and 22. Figs. 23 and 24 are presentations of the heat extraction efficiency curves based on Model 1 under the under the pressure boundary conditions $\Delta p = 0.98$ and 2.94 MPa. It is found that there is no hump on the heat extraction curves in Fig. 23. The reason is that the reservoir temperature does not reach critical values that allow appearances of humps on the heat extraction curves. In contrast, the humps on the heat extraction curves can be observed in Fig. 24.

The cumulative heat production and heat extraction efficiencies for four chosen proportions (90% CO_2 and 10% N_2, 80% CO_2 and 20% N_2, 70% CO_2 and 30% N_2, 60% CO_2 and 40% N_2) under three pressure boundary conditions ($\Delta p = 0.98$, 1.96 and 2.94 MPa) are shown in Figs. 25 and 26. Figs. 25 and 26 provide direct comparisons among three pressure boundary conditions and are used to validate the effects of reservoir pressure conditions on the appearance of humps on the heat extraction curves. Based on the above analysis in Figs. 17–26, it is proved that the optimized heat extraction efficiency range exists and indicated that the working fluid properties and reservoir temperature have direct effects on the optimized heat extraction efficiency range.

5. Conclusions

In this study, a miscible injection of CO_2 and N_2, a novel working fluid, is proposed. On the basis of initial model setup and relevant assumptions, with the injection of CO_2 and N_2 miscible flow, the EGS model that integrates the discrete fracture network model and the thermal-hydraulic-mechanical coupling mechanisms have been successfully developed and evaluated.

Simulation results show that different CO_2 and N_2 proportions in the miscible flow have predictable effects on the heat extraction from geothermal reservoirs. It can be observed that the heat extraction curves of proportions (60% CO_2 and 40% N_2, 80% CO_2 and 20% N_2) have similar characteristics in being higher than corresponding curves of other proportions, which indicates that the miscible flow with the above proportions is a more efficient working fluids in most times. It is concluded that heat extraction efficiencies have no positive relationships with the increasing proportions of N_2 in miscible flow though larger proportions of N_2 can reduce the densities, viscosities and even heat capacities of the miscible flow to certain extent. Based on simulation results and corresponding analysis, the miscible flow with ten CO_2 and N_2 proportions can be divided into top, middle and bottom part. The trends and distributions of permeability and effective normal stress curves strictly correspond to those of the heat extraction curves.

The heat extraction efficiencies for the miscible flow with different proportions have been evaluated in a period of 20 years. It is found that humps that appear on the heat extraction efficiency curves means higher heat extraction efficiencies for a period, which can be described as reasonable ranges that produce geothermal energy from deep reservoirs more efficiently. Under the conditions of this study, the impacting factors, including boundary conditions, fluids properties and the discrete fracture network, have been investigated. It is found that larger pressure differences between the inlet and outlet boundaries lead to earlier appearances of humps on the heat extraction efficiency. Different working fluids properties due to different CO_2 and N_2 proportions have direct effects on the appearance of humps. Small differences exist between two discrete fracture network models due to different hydraulic conductivities that are determined by discrete fracture networks. Because the conductivities of fracture networks and pressure boundary conditions affect heat extraction from the reservoir and consequently the reservoir temperature, it is concluded that the reservoir temperature also influences the optimized heat extraction range directly.

Simulation results are validated through mutual comparisons between two different discrete fracture network models. This study proposes a novel working fluid for the EGS model and suggests a reasonable range for more efficient heat extraction and a new concept of the optimized heat extraction efficiency range. This will contribute to the application of different working fluids with considering both heat extraction efficiency and the amount of CO_2 storage and optimized production plans of geothermal projects.

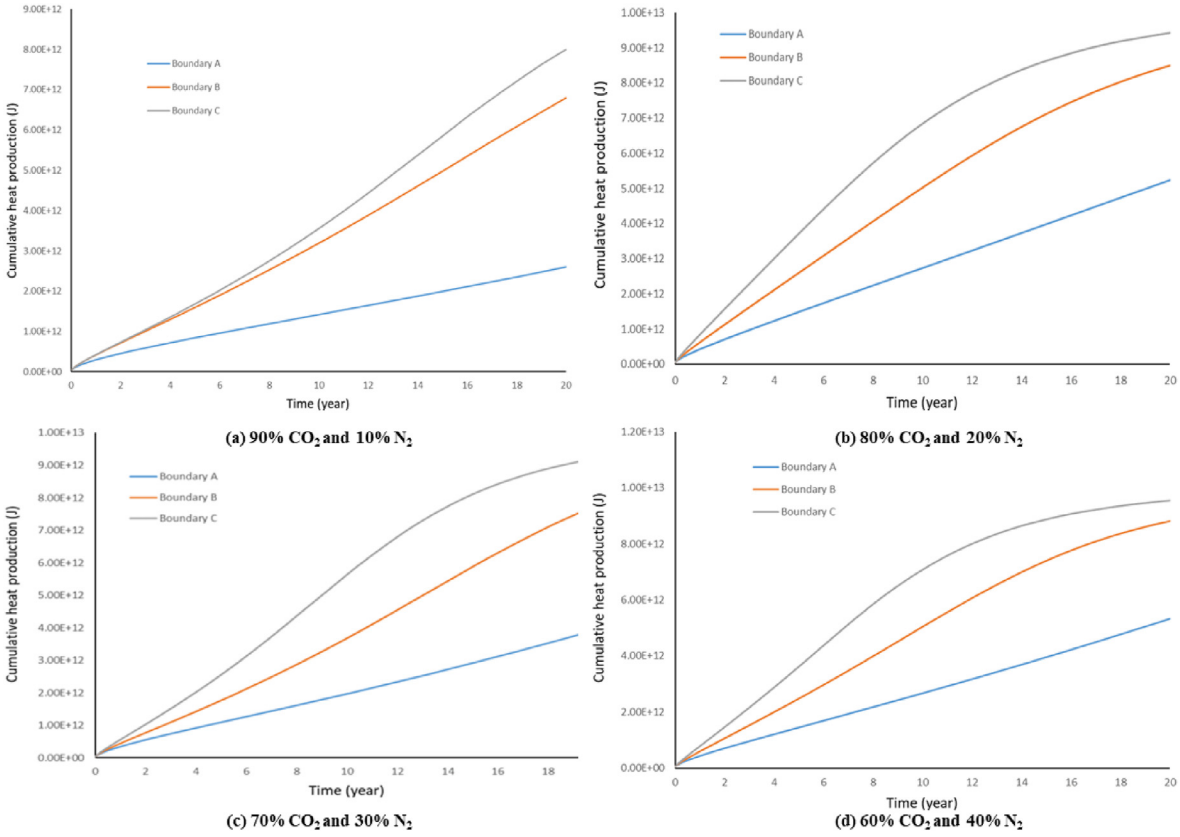

Fig. 25. Cumulative heat production based on Model 1with different pressure conditions: Boundary A Δp = 0.98 MPa; Boundary B Δp = 1.96 MPa; Boundary C Δp = 2.94 MPa.

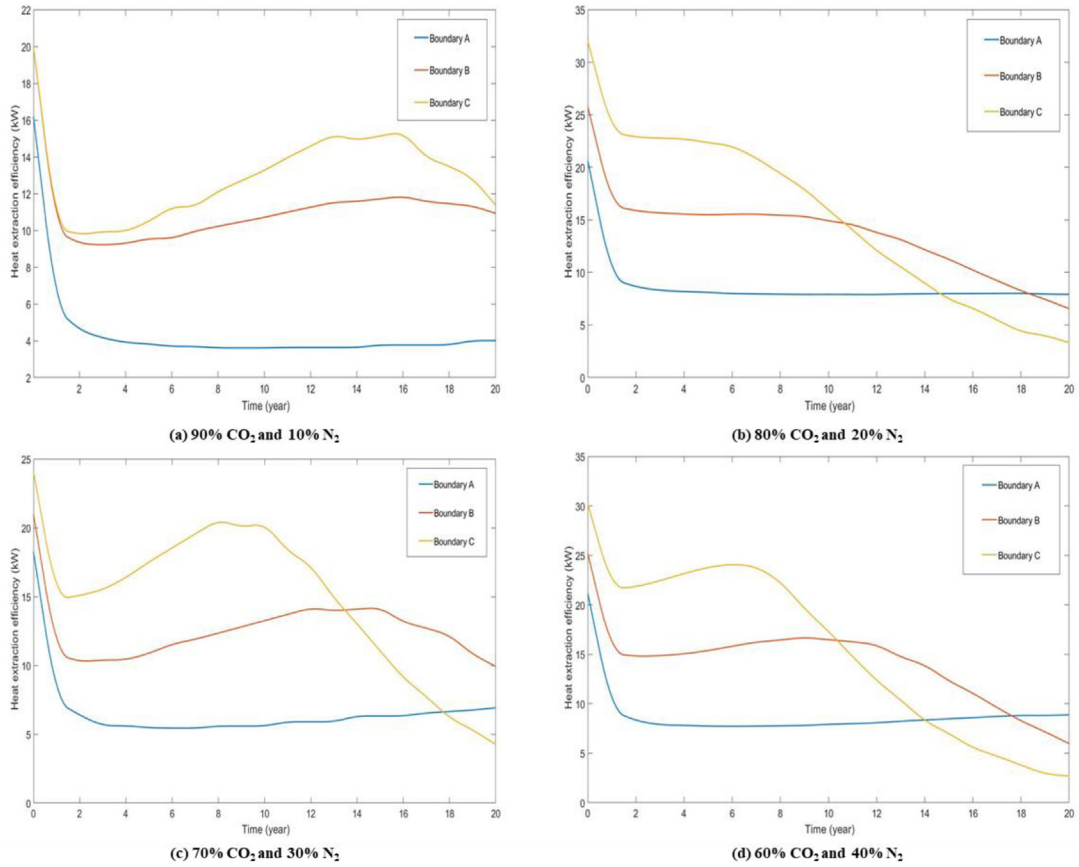

Fig. 26. Heat extraction efficiency based on Model 1with different pressure conditions: Boundary A Δp = 0.98 MPa; Boundary B Δp = 1.96 MPa; Boundary C Δp = 2.94 MPa.

CRediT authorship contribution statement

Jiawei Li: Conceptualization, Methodology, Formal analysis, Writing - original draft. **Wanju Yuan:** Data curation. **Yin Zhang:** Formal analysis. **Claudia Cherubini:** Writing - review & editing. **Alexander Scheuermann:** Writing - review & editing. **Sergio Andres Galindo Torres:** Writing - review & editing. **Ling Li:** Writing - review & editing.

Declaration of competing interest

We declare that we have no financial and personal relationships with other people or organizations that can inappropriately influence our work, there is no professional or other personal interest of any nature or kind in any product, service and/or company that could be construed as influencing the position presented in, or the review of, the manuscript "Numerical Investigations of CO_2 and N_2 miscible flow as the working fluid in Enhanced Geothermal Systems".

References

[1] BP plc. BP 2017 statistical review of of world energy. June 2018.
[2] Global CCS Institute, The global status of CCS 2013.
[3] Geothermal Energy Association. 2016 annual U.S. & global geothermal power production report. 2016. Washington, D.C.
[4] Brown DW. A hot dry rock geothermal energy concept utilizing supercritical CO_2 instead of water. January 24-26. In: Proceedings of the twenty-fifth workshop on geothermal reservoir engineering. CA: Stanford University; 2000. SGP-TR-165.
[5] Pruess K. Enhanced geothermal systems (EGS) using CO_2 as working fluid – a novel approach for generating renewable energy with simultaneous sequestration of carbon. Geothermics 2006;35:351–67.
[6] Xu RN, Zhang L, Zhang FZ, Jiang PX. A Review on heat transfer and energy conversion in the enhanced geothermal systems with water/CO_2 as working fluid. Int J Energy Res 2015;39(13):1722–41.
[7] Harto C, Schroeder J, Martino L, Horner R, Clark C. Geothermal energy: the energy-water nexus. In: Proceedings of 38th workshop on geothermal reservoir engineering. Stanford, CA: SGP-TR-198; 2013.
[8] Harto C, Schroeder J, Martino L, Horner R, Clark C. Geothermal energy: the energy-water nexus. In: Proceedings of 38th workshop on geothermal reservoir engineering. Stanford, CA: SGP-TR-198; 2013.
[9] Pruess K. Enhanced geothermal systems (EGS) using CO2 as working fluid – a novel approach for generating renewable energy with simultaneous sequestration of carbon. Geothermics 2006;35:351–67.
[10] Fouillac C, Sanjuan B, Gentier S, Czernichowski-Lauriol I. Could sequestration of CO_2 be combined with the development of enhanced geothermal systems?. In: Third annual conference on carbon capture and sequestration; May 3-6, 2004. Alexandria, vol. A.
[11] Global CCS Institute. reportIntroduction to carbon capture and storage. Global status of CCS 2016: special report.
[12] Buscheck TA, Bielicki JM, Randolph JB, Chen M, Hao Y, Edmunds TA, Adams B, Sun Y. Multi-fluid geothermal energy systems in stratigraphic reservoirs: using brine, N_2, and CO_2 for dispatchable renewable power generation and bulk energy storage. In: Proceedings of the 39th workshop on geothermal reservoir engineering. Palo Alto, CA: Stanford University; 2014.
[13] Buscheck TA, Bielicki JM, Chen M, Sun YW, Hao Y, Edmunds TA, Randolph JB, Saar MO. Multi-fluid sedimentary geothermal energy systems for dispatchable renewable electricity. In: Proceedings world geothermal congress; 2015. Melbourne, Australia, April 19-25.
[14] Xu TF, Pruess K, Apps J. Numerical studies of fluid-rock interactions in Enhanced Geothermal Systems (EGS) with CO_2 as working fluid. January 28–30. In: Proceedings of the thirty-third workshop on geothermal reservoir engineering. Stanford, CA: Stanford University; 2008. SGP-TR-185.
[15] Olasolo P, Juárez MC, Morales MP, Sebastiano DA, Liarte IA. Enhanced geothermal systems (EGS): a review. Renew Sustain Energy Rev 2016;56:133–44.
[16] Zhang FZ, Jiang PX, Xu RN. System thermodynamic performance comparison of CO2-EGS and water-EGS systems. Appl Therm Eng 2013;61:236–44.
[17] Borgia A, Oldenburg CM, Zhang R, Pan LH, Daley TM, Finsterle S, Ramakrishnan TS. Simulation of CO_2 injection into fractures and faults for improving their geophysical characterization at EGS sites. Geothermics 2017;69:189–201.
[18] Xu TF, Pruess K, Apps J. Numerical studies of fluid-rock interactions in Enhanced Geothermal Systems (EGS) with CO_2 as working fluid. January 28–30. In: Proceedings of the thirty-third workshop on geothermal reservoir engineering. Stanford, CA: Stanford University; 2008. SGP-TR-185.
[19] Borgia A, Pruess K, Kneafsey TJ, Oldenburg CM, Pan l. Numerical simulation of salt precipitation in a fractured CO_2-Enhanced geothermal system. Geothermics 2012;44:13–22.
[20] Li JW, Sun ZX, Jiang CY, Cherubini C, Scheuermann A, Galindo Torres SA, Li L. Investigations of heat extraction for water and CO_2 flow based on the rough-walled discrete fracture network. Energy 2019;189:116184.
[21] Song XZ, Shi S, Li GS, Yang RY, Wang GS, Zhang R, Li JC, Lyu ZH. Numerical simulation of heat extraction performance in enhanced geothermal system with multilateral wells. Appl Energy 2018;218:325–37.
[22] Huang WB, Cao WJ, Jiang FM. Heat extraction performance of EGS with heterogeneous reservoir: a numerical evaluation. Int J Heat Mass Tran 2017;108:645–57.
[23] Juliusson E, Horne RN. Optimization of injection scheduling in fractured geothermal reservoirs. Geothermics 2013;48:80–92.
[24] Milan JP, l Eric FM, Michael LJ. High-fidelity reservoir simulations of enhanced gas recovery with supercritical CO_2. Energy 2016;111:548–59.
[25] Global CCS Institute. reportIntroduction to industrial carbon capture and storage. Global Status of CCS 2016: special Report.
[26] Omar E, Haitham AR, Frede B. Renewable energy resources: current status, future prospects and their enabling technology. Renew Sustain Energy Rev 2014;39:748–64.
[27] Adams BM, Kuehn TH, Bielicki JM, et al. A comparison of electric power output of CO_2 Plume Geothermal (CPG) and brine geothermal systems for varying reservoir conditions. Appl Energy 2015;140:365–77.
[28] Garapati N, Randolph JB, Saar MO. CO_2-Plume based geothermal (CPG) heat extraction in multi-layered geologic reservoirs. Energy Procedia 2014;63:7631–43.
[29] Cui GD, Wang Y, Rui ZH, Chen BL, Ren SR, Zhang L. The influence of complicated fluid-rock interactions on the geothermal exploitation in the CO_2 plume geothermal system. Appl Energy 2018;227:49–63.
[30] Tudor R, Vozniak C, Peters W, Banks ML. Technical advances in liquid CO_2 fracturing. In: Annual technical meeting, june 12 - 15; 1994. Calgary, Alberta. PETSOC-94-36.
[31] Zhang XW, Lu YY, Tang JR, Zhou Z, Liao Y. Experimental study on fracture initiation and propagation in shale using supercritical carbon dioxide fracturing. Fuel 2017;190:370–8.
[32] Michael GT, Richard EM. A comparison of results of three different CO_2 energized frac fluids: a case history. April 30-May 2. In: SPE gas technology symposium. Calgary, Alberta: Canada; 2002. SPE-75681-MS.
[33] Zhang L, Jiang PX, Wang ZC, Xu RN. Convective heat transfer of supercritical CO2 in a rock fracture for enhanced geothermal systems. Appl Therm Eng 2017;115:923–36.
[34] Sun XH, Wang ZY, Sun BJ, Wang WD. Research on hydrate formation rules in the formations for liquid CO_2 fracturing. J Nat Gas Sci Eng 2016;33:1390–401.
[35] Wang F, Fu SF, Guo G, Jia ZZ, Luo SJ, Guo RB. Experimental study on hydrate-based CO_2 removal from CH_4/CO_2 mixture. Energy 2016;104:76–84.
[36] Liu YG, Hou J, Zhao HF, Liu XY, Xia ZZ. A method to recover natural gas hydrates with geothermal energy conveyed by CO_2. Energy 2018;144:265–78.
[37] Alvarado V, Manrique E. Enhanced oil recovery: an update review. Energies 2010;3:1529–75.
[38] Blunt M, Fayers FJ, Orr Jr FM. Carbon dioxide in enhanced oil recovery. Energy Convers Manag 1993;34(9–11):1197–204.
[39] Gozalpour F, Ren SR, Tohidi B. CO2 EOR and storage in oil reservoir. Oil Gas Sci Technol 2005;60(3):537–46.
[40] Oldenburg CM, Pruess K, Benson SM. Process modeling of CO_2 injection into natural gas reservoirs for carbon sequestration and enhanced gas recovery. Energy Fuels 2001;15:293–8.
[41] Cui X, Bustin RM, Dipple G. Selective transport of CO_2, CH_4, and N_2 in coals: insights from modeling of experimental gas adsorption data. Fuel 2004;83(3):293–303.
[42] Thomas S. Enhanced oil recovery – an overview. Oil Gas Sci Technol 2008;63:9–19.
[43] Vicencio OA, Sepehrnoori K. Simulation of nitrogen injection into naturally fractured reservoirs. Mexico, November 7-9. In: SPE international petroleum conference; 2004. SPE-92110-MS.
[44] Bahralolom IM, Orr Jr FM. Solubility and extraction in multiple contact miscible displacements: comparison of N_2 and CO_2 flow visualization experiments. 01 SPE Reservoir Eng 1988;3. SPE-15079-PA.
[45] Hassan M, Gajbhiye R. Performance of CO_2/N_2 foam in enhanced oil recovery. SPE-191208-MS. In: SPE Trinidad and Tobago section energy resources conference, Trinidad and Tobago; 2018. Spain, June 25-26.
[46] Belhaj H, Abukhalifeh H, Javid K. Miscible oil recovery utilizing N_2 and/or HC gases in CO_2 injection. J Petrol Sci Eng 2013;111:144–52.
[47] Seomoon H, Lee M, Sung W. Analysis of methane recovery through CO_2–N_2 mixed gas injection considering gas diffusion phenomenon in coal seam. Energy Explor Exploit 2016;34(5):661–75.
[48] Shukla R, Ranjith P, Haque A, Choi X. A review of studies on CO_2 sequestration and caprock integrity. Fuel 2010;89(10):2651–64.
[49] Rubin E, Meyer L, Coninck H. IPCC special report on carbon dioxide capture and storage; prepared by working group III of the intergovernmental panel on climate change. Cambridge, UK: Intergovernmental Panel on Climate Change; 2005.
[50] Agartan E, Gaddipati M, Yip Y, Savage B, Ozgen C. CO_2 storage in depleted oil and gas fields in the Gulf of Mexico. International Journal of Green Gas Control 2018;72:38–48.
[51] Jessen K, Kovscek AR, Orr Jr FM. Increasing CO_2 storage in oil recovery. Energy

Convers Manag 2005;46(2):293–311.
[52] Zhang L, Ezekiel J, Li D, et al. Potential assessment of CO_2 injection for heat mining and geological storage in geothermal reservoirs of China. Appl Energy 2014;122:237–46.
[53] Randolph JB, Saar MO. Combining geothermal energy capture with geologic carbon dioxide sequestration. Geophys Res Lett 2011;38:10401.
[54] Olasolo P, Juarez MC, Morales MP, D'Amico S, Liarte IA. Enhanced geothermal systems (EGS): a review. Renew Sustain Energy Rev 2016;56:133–44.
[55] Assessing the earthquake risk of enhanced geothermal Systems. Power; 2009.
[56] Liang B, Jiang HQ, Li JJ, Gong CC. A systematic study of fracture parameters effect on fracture network permeability based on discrete-fracture model employing finite element analyses. J Nat Gas Sci Eng 2016;28:711–22.
[57] Saeid S, Al-Khoury R, Barends F. An efficient computational model for deep low-enthalpy geothermal systems. Comput Geosci 2013;51:400–9.
[58] Xu C, Dowd PA, Zhao FT. A simplified coupled hydro-thermal model for enhanced geothermal systems. Appl Energy 2015;140:135–45.
[59] Chen BG, Song EX, Cheng XH. A numerical method for discrete fracture network model for flow and heat transfer in two-dimensional fractured rocks. Chin J Rock Mech Eng 2014;33(1):43–51 [in Chinese)].
[60] Zhao YS, Feng Z, Yang D, Liang W. THM (Thermo-hydro-mechanical) coupled mathematical model of fractured media and numerical simulation of a 3D enhanced geothermal system at 573 K and buried depth 6000–7000 M. Energy 2015;82:193–205.
[61] Gisladottir VR, Roubinet D, Tartakovsky M. Particle methods for heat transfer in fractured media. Transport Porous Media 2016;115:311–26.